AIAA 2003-4406

Propulsion Airframe Integration Test Techniques for Hypersonic Airbreathing Configurations at NASA Langley Research Center (Invited)

David W. Witte, Lawrence D. Huebner, Carl A. Trexler, and Karen F. Cabell
NASA Langley Research Center
Hampton, VA

Earl H. Andrews, Jr.
Swales Aerospace
Hampton, VA

39th AIAA/ASME/SAE/ASEE Joint Propulsion Conference
July 20-23, 2003
Huntsville, Alabama

39th AIAA/ASME/SAE/ASEE Joint Propulsion Conference
Huntsville, Alabama
July 20-23, 2003

PROPULSION AIRFRAME INTEGRATION TEST TECHNIQUES FOR HYPERSONIC AIRBREATHING CONFIGURATIONS AT NASA LANGLEY RESEARCH CENTER (INVITED)

David W. Witte, Lawrence D.Huebner, Carl A. Trexler, and Karen F. Cabell

Hypersonic Airbreathing Propulsion Branch
NASA Langley Research Center
Hampton, VA 23681

Earl Andrews

Swales Aerospace
Hampton, VA 23681

ABSTRACT

The scope and significance of propulsion airframe integration (PAI) for hypersonic airbreathing vehicles is presented through a discussion of the PAI test techniques utilized at NASA Langley Research Center. Four primary types of PAI model tests utilized at NASA Langley for hypersonic airbreathing vehicles are discussed. The four types of PAI test models examined are the forebody/inlet test model, the partial-width/truncated propulsion flowpath test model, the powered exhaust simulation test model, and the full-length/width propulsion flowpath test model. The test technique for each of these four types of PAI test models is described, and the relevant PAI issues addressed by each test technique are illustrated through the presentation of recent PAI test data.

Nomenclature

AF	axial force
ATE	aftbody trailing edge
C_A	axial force coefficient
C_D	drag coefficient
C_L	lift coefficient
C_M	pitch moment coefficient
C_N	normal force coefficient
C_P	pressure coefficient
NF	normal force
M	Mach number
P	static pressure
PM	pitch moment
q	dynamic pressure
SNPR	static nozzle pressure ratio
Xaft	axial distance from CTE
α, AOA	angle of attack
γ	ratio of specific heats

Subscripts

as	aerodynamic surfaces
aps	aerodynamic and propulsion surfaces
BP	back pressure
CLE	cowl leading edge
CTE	cowl trailing edge
inf	freestream location
2	flow conditions downstream of model leading edge shock
4	CTE station

INTRODUCTION

NASA is using the X-43 series of experimental aircraft (X-43A, X-43B, X-43C, and X-43D)[1] to conduct research into hypersonic airbreathing vehicle design. These flight research aircraft utilize scramjet engines, integrated into the airframe of the vehicle. Such engine installations are referred to as airframe-integrated scramjets. This is to distinguish them from first generation, axisymmetric strut-mounted scramjet designs such as the NASA Hypersonic Research Engine, HRE[2]. Strut-mounted scramjet designs were found to incur very severe shock interaction heating and aerodynamic drag. As a result, the airframe-integrated scramjet design was developed to avoid/minimize such problems. An example of an aircraft employing an airframe-integrated scramjet is presented in Fig. 1. With this type of vehicle, the integration of the propulsion system (scramjet) with the airframe becomes integral to the vehicle design. This integration is referred to as propulsion airframe integration, PAI. The primary PAI issues for an airframe-integrated scramjet-powered aircraft (noted in Fig.1) are the forebody inlet interactions, the exhaust jet interactions with the external nozzle and control surfaces of the aftbody, and the propulsion control system interactions with the vehicle control system.

In the design and development stage for a hypersonic airbreathing vehicle (such as the X-43A, B, C, or D), a number of ground test models are built and wind tunnel tested to validate the vehicle design and verify its predicted performance.[3] These ground tests are designed specifically to address the aerodynamics, propulsion, and PAI issues/performance for the flight vehicle. With regard to PAI, there are four primary types of test models that are utilized at NASA Langley Research Center (LaRC) for hypersonic airbreathing configurations. They are most commonly referred to as: forebody/inlet test models, partial-width/truncated propulsion flowpath test models, powered exhaust simulation test models, and full-length/width propulsion flowpath test models. In this paper, the test technique for each of these four types of PAI test models will be described. In addition, the relevant PAI issues addressed by each test technique will be illustrated through the presentation of recent PAI test data. The intent is to provide the reader with an understanding of the scope and significance of PAI for hypersonic airbreathing vehicles, through the discussion of the PAI test techniques utilized at Langley Research Center for such vehicles.

FOREBODY/INLET TESTS

Technique Description

From a PAI perspective, forebody/inlet tests are utilized to determine the effect of the forebody-processed flow on the inlet performance. Fig. 2 shows a forebody inlet model, mounted inverted, used for the X-43C project.[4] This model represents a two-dimensional simulation of the flow through the center module of the three-module X-43C vehicle. It was tested in the Langley Mach 4 Blow Down Facility (M4BDF), which has been used extensively for research and performance verification of forebody/inlet designs of airframe-integrated scramjet-powered vehicle concepts. Fig. 3 illustrates how the simulation of the flow into the inlet is accomplished. The location of Mach 4 flow on the X-43C vehicle is first determined from oblique shock theory or CFD. This point on the X-43C represents the starting point or leading edge for the forebody/inlet model. With this leading edge selection, the M4BDF nozzle flow can be used as a freestream flow for this forebody/inlet model. This truncated forebody approach has two major benefits. First, it allows a lower Mach number facility, with lower test-gas heating requirements, to be used. Lower test gas heating requirements also translate into less stringent thermal design requirements for the test model. Second, it allows for a larger scale model to be built for a given test facility. Schematics of the planform and profile views for this X-43C forebody/inlet model with an attached flow meter are given in Fig. 4. In the planform view, the spatula shaped forebody illustrates how the two-dimensional flow simulation to the inlet is accomplished, by preventing forebody edge effects from being captured by the inlet. In the profile view, the mechanical operational limits of the cowl flap and mass flow meter for this model are shown. The cowl flap actuation allows for inlet contraction ratio variation during a run while the flow meter actuation allows for back-pressure variation. Also in the profile view, a boundary layer plate is shown installed in front of the leading edge of the forebody. This boundary layer plate is used to generate a more realistic forebody boundary layer thickness at the entrance to the inlet.

The major PAI issues addressed with the forebody/inlet test models are the effects of the forebody boundary layer, the inlet mass capture, and the limits for the inlet starting, unstart contraction ratio, unstart backpressure, and unstart loads. These test models can be used to investigate effects of boundary layer height by the attachment of a boundary layer plate of specified length. Through the addition of boundary layer trips, they can also be used to assess the effect of the boundary layer state (laminar, transitional, or turbulent). Finally, through the use of active boundary layer control techniques, such as mass injection, they can also be used to study transition location effects. Mass capture effects, which may be varied via cowl flap angle, are evaluated from the model flow meter mass flow measurements. The unstart loads, both static and dynamic, on the body and cowl side of the inlet can be evaluated from inducing either a contraction ratio or a backpressure unstart. The limits for both inlet self-starting and contraction ratio unstarts can be determined from cowl flap actuation during a run, while the flow meter actuation allows for determination of the backpressure unstart limit.

Illustration of PAI Effects

Fig. 5 shows some schlieren photographs of the X-43C forebody/inlet model in the M4BDF. These results are for the test model both with and without the boundary layer plate to provide some insight into the boundary layer effects. The top pair of images are for the no flow condition, and are provided for reference. The middle pair of images, for a started inlet test point, indicates that the boundary layer plate generates an obviously larger boundary layer. The lower pair of images shows a similar unstarted inlet flow structure for the forebody, but the boundary layer plate configuration unstarted at a much lower contraction ratio. This implies a

significant lower mass capture limit with a full forebody boundary layer. A sample of the body side pressure data acquired from this X-43C forebody/inlet model is provided in Fig. 6. Static pressure distribution results are shown for a minimum backpressure (mass flow meter full open) started inlet, for a maximum backpressure started inlet, and for an unstarted inlet. Dynamic (high frequency, HF) unstarted inlet pressure data from three dynamic pressure transducers are represented by the three large yellow diamonds. This plot reveals that dynamic unstart pressures can be several times the value of the static unstart pressures, indicating the importance of performing a dynamic load analysis with the design of the inlet.

A forebody/inlet model of a different type of airframe-integrated scramjet vehicle concept is presented in Fig. 7. Known as the REST (Rectangular-to-Elliptical Shaped-Transition) concept[5], this represents a vehicle design incorporating two-dimensional forebody flow and elliptical combustor flow, with the inlet providing the transition from a rectangular forebody shape to an elliptical combustor shape. This REST concept is a clear example of PAI incorporated into the vehicle design, allowing a desired two-dimensional forebody from an airframe standpoint, to be mated with a desired round-shaped (elliptical) combustor from a propulsion and structural standpoint.

Another type of hypersonic airbreathing vehicle design, known as a Turbine-Based Combined Cycle, TBCC, dual (over/under) flowpath concept is presented in Fig. 8. This concept has a low-speed turbine engine flowpath mounted above a high-speed scramjet flowpath. To evaluate the inlet performance and operability limits for this concept, a forebody/inlet model is currently being designed and fabricated at NASA Langley Research Center for an upcoming test entry into the M4BDF. The planform and profile schematics for this forebody/inlet model are shown in Fig. 9. This forebody/inlet model is also tested inverted in the M4BDF. The model will have the ability to actuate both the low-speed and high-speed cowl flap during a run to enable investigation of the effect of the low-speed cowl flap position on the high-speed inlet performance and operability limits. Fig. 10 illustrates one of the primary concerns with the inlet design for this concept. The location of the low-speed cowl flap hinge point determines the origination point for the initial high-speed inlet shock while the contraction ratio for this low-speed inlet determines the strength of this initial high-speed inlet shock. The PAI complexity here is essentially doubled with the presence of two propulsion flowpaths.

PARTIAL-WIDTH/TRUNCATED PROPULSION FLOWPATH TESTS

Technique Description

The partial-width/truncated propulsion flowpath tests are used to address the PAI effects of the forebody processed flow on the entire internal propulsion flowpath (inlet, isolator, combustor, and internal nozzle). While this model can and is used to assess inlet PAI issues, the majority of inlet PAI investigation is performed with the forebody/inlet model because of the significantly lower model and facility costs for these tests. An X-43A (Hyper-X)[6] partial-width/truncated propulsion flowpath test model, known as the DFX model, is shown in Fig. 11 in the test section of the Langley Arc Heated Scramjet Test Facility (AHSTF)[7]. The DFX had a truncated forebody and truncated aftbody compared to the full length of the Hyper-X. It also had a partial-width flowpath compared to that of the Hyper-X. A planform overlay of the DFX on the underside of the Hyper-X is provided in Fig. 12, clearly showing the truncated length and partial-width of this test model. Also, shown in Fig. 12 is the freestream flow simulation technique employed. The DFX was positioned in the AHSTF at a model rotation angle that produced the same M_2 (Mach number downstream of the shock from the model leading edge) from the Mach 6.2 facility nozzle exit flow as the M_2 for the flight vehicle at Mach 7. With this test technique, it is possible to match the enthalpy and dynamic pressure of the facility nozzle flow delivered to the test model to flight values. Facility limitations prevented a dynamic pressure simulation for this test. Truncating the model length and making it partial-width allow for a larger scale model to be tested with this technique. With the DFX, this truncation enabled the testing of a full-scale (length and height) Hyper-X internal propulsion flowpath model in the AHSTF.

The range of PAI issues that can be addressed with this partial-width/truncated propulsion flowpath test model include forebody boundary layer effects, inlet mass capture effects, inlet/isolator operability limits, internal propulsion flowpath thrust performance, and propulsion system control effects. The same techniques used for investigating boundary layer and inlet mass capture effects with the forebody/inlet test models, described earlier, are applicable here.

Two sets of boundary layer trips that were developed and tested for the Hyper-X program are shown in Fig. 13. These trips were tested on a partial-width/truncated propulsion flowpath test model known as the Hyper-X

Engine Model, HXEM. Pitot pressure results near the inlet entrance plane for these trips, presented in Fig. 14, indicated negligible difference between the trip designs and only a small difference compared to no trips. This indicates that this facility is delivering a nearly fully turbulent boundary layer to the model. This differs from flight conditions where a laminar boundary layer could persist. The boundary layer trips are required to force the boundary layer to become turbulent before entering the engine inlet in order to decrease the likelihood of boundary layer separation within the inlet.

The effect of boundary layer height on internal propulsion flowpath performance was investigated with the HXEM, by diverting the boundary layer from the forward section of the forebody. Fig. 15 shows the HXEM without forebody boundary layer diversion and Fig. 16 shows the HXEM configured with forebody boundary layer diversion.

An assessment of the forebody-produced, cowl leading edge (CLE) Mach number, M_{CLE}, on the internal propulsion flowpath performance was accomplished during the HXEM test entry in the AHSTF. Fig. 17 illustrates how changing the HXEM model rotation angle from 0 to –6 degrees resulted in a M_{CLE} variation from 4.6 to 5.3.

The set of forebody flow survey rakes used to determine inlet mass capture for the HXEM test entry in the Langley 8-Ft. High Temperature Tunnel, 8-Ft. HTT,[8] are shown in Fig. 18. The data from these flowfield surveys were used to compute the local mass flux. The local mass flux values were then integrated, out to the stream lines defining the capture box for the inlet (using CFD), to determine the inlet mass capture.

Fig. 19 represents the fuel and ignitor sequence for the Hyper-X vehicle, which was verified with tests of the HXEM. The effects of fuel flow rates on the isolator interaction for a given isolator entrance flow (resulting from a specified cowl flap angle and forebody flow) were assessed.

Illustration of PAI Effects

Due to the classified nature of the internal propulsion flowpath data, no example data results can be presented in this paper.

POWERED EXHAUST SIMULATION TESTS

Technique Description

Powered exhaust simulation test models are used to study the hypersonic airbreathing vehicle PAI issue of engine exhaust jet interaction with the external nozzle and control surfaces of the vehicle aftbody. An example of a powered exhaust simulation test model is presented in Fig. 20. This model, known as Model 5B, was a scale model of the National Aero-Space Plane (NASP) vehicle, also known as the X-30.[9] Powered exhaust simulation test models such as Model 5B are subscale to enable testing in the full range of hypersonic wind tunnels. Because these models just simulate the engine exhaust, no actual flowpath combustion is required, and therefore minimum model size requirements (resulting from combustor flow residence time concerns) do not exist. Specifically, Model 5B was tested at NASA Langley in the 16-Foot Transonic Tunnel between Mach 0.7 to 1.2, in the Unitary Wind Tunnel at Mach 3.4, in the 20-Inch Mach 6 Wind Tunnel, and the 31-Inch Mach 10 Wind Tunnel. [10, 11, 12]

Fig. 21 shows a profile schematic of Model 5B revealing all of its major internal features. The model was strut-mounted to its forebody upper surface. The strut, in addition to acting as a mounting support, provided the delivery passage for the simulant exhaust gas to the model, as well as the instrumentation cavity. The simulant exhaust gas was piped into a plenum within the model forebody and then expanded through a supersonic nozzle, designed to simulate the target exit Mach number for the NASP engine at a specified flight condition. For Model 5B, two simulant exhaust gases were employed during testing. For cost effectiveness, most of the testing was conducted using air as the simulant exhaust gas. To investigate the effects of an exhaust gas with a low ratio of specific heats (γ) that is more representative of hot combustion products, a 70/30 mole fraction mixture of CF_4/Ar was also employed as a simulant exhaust gas. The inlet for Model 5B was faired-over. The aftbody of this model possessed a metric break and was attached to the forebody via a six-component strain gauge balance for force and moment measurements. A teflon seal installed in the metric gap prevented the high pressure nozzle exhaust from pressurizing the front, internal base area of the aftbody. A separate high-density, pressure-instrumented aftbody could be interchanged for the metric force-and-moment aftbody to enable determination of the pressure distribution on the external nozzle surface. Model 5B also had pressure-instrumented horizontal tails and body flaps for

examination of the exhaust jet effect on these control surfaces. The cowl external surface was also pressure-instrumented for measurement of the exhaust jet effect on this surface.

With this test technique, four key parameters need to be appropriately reproduced in order to accomplish a correct force and moment simulation of a scramjet exhaust flow field. They are, geometric similarity for the internal and external nozzles, the internal nozzle exit Mach number (M_4), the static nozzle pressure ratio (referred to as SNPR) defined as the internal nozzle exit static pressure (P_4) divided by the freestream static pressure (P_{inf}), and γ for the entire exhaust flow field. Essentially, Mach number and γ determine the expansion characteristics for any nozzle flow, thereby generating the requirement for a M_4 and γ_4 match. Of course, while it is self evident why the nozzle geometry must also be similar to match the exhaust flow expansion characteristics, the exhaust plume constitutes the lower surface nozzle geometry. The correct reproduction of the exhaust plume boundary is accomplished by matching the correct SNPR.

The jet-effect on the external nozzle and control surfaces of the aftbody is obtained by computing the difference between acquired data at unpowered (jet-off) and powered (jet-on) conditions. The forebody strut mounting is assumed to affect the absolute magnitude of the measured aftbody forces and moments, because of the flow disturbance that it causes significantly affects the flow along the upper surface of the aftbody. However, the measured jet-effect is not affected by the strut because only the upper surface is assumed to be impacted by the strut, and the exhaust plume does not affect the upper surface. In the NASP force accounting methodology, the aftbody jet-effect data was to be added to unpowered aerodynamic model test data. This combined data, in conjunction with internal propulsion flowpath test data, would enable the determination of installed performance for the vehicle.

The jet-effect on the control surface effectiveness (delta C_M/degree deflection) of the horizontal tails and body flaps represent another aspect of aftbody PAI for hypersonic airbreathing vehicles. This jet-effect is determined by the difference between the powered and unpowered control surface effectiveness (where control surface effectiveness is determined from aftbody data across the range of control surface deflections). This jet-effect on control surface effectiveness is added to the unpowered aerodynamic model control surface effectiveness value to arrive at an installed performance value of control effectiveness for the horizontal tails and body flaps. Depending on the design of the aftbody, the jet-effect on the control surface effectiveness can be significant for hypersonic airbreathing vehicles. This issue impacts not only the vehicle stability but also the vehicle flight control system design. One final PAI consideration with regard to control surface effectiveness is the trim drag penalty incurred for deflections of the control surfaces. The main issue here is simply whether the vehicle design has enough thrust margin to overcome the drag penalty for trimmed flight, in order to maintain acceleration throughout the designed speed regime of the vehicle.

Illustration of PAI Effects

The primary aftbody exhaust flow structures for a hypersonic airbreathing vehicle are seen in the Schleiren photograph of Model 5B (Fig. 22) in the Unitary Plan Wind Tunnel at Mach 3.4. An exhaust plume emanating from the cowl trailing edge extends downward below the plane of the cowl external surface. This was the case for all tested conditions at Mach 3.4, 6, and 10 with Model 5B. It was a result of all SNPR values for these tests being greater than one (under-expanded flow), causing the exhaust jet to plume outward into the cowl external flowfield. An external plume shock is generated from the interaction of the external flow, below the cowl, with the exhaust plume. As the internal exhaust flow starts an expansion turn at the cowl trailing edge it immediately collides with the exhaust plume generating the observed internal plume shock. Although this Schlieren photograph only shows the profile flow features, similar exhaust plume expansion and shock structure occurs in the spanwise direction because this aftbody exhaust flowfield is very three-dimensional. Fig. 23, a set of rear view, vapor screen images from Model 5B at Mach 3.4, illustrates the spanwise features of the aftbody flowfield. Vapor screen photographs were recorded at five separate axial locations along the aftbody for both the jet-off and a nominal jet-on condition. Aftbody station number 1 was at the cowl trailing edge (CTE) and aftbody station number 5 was at the aftbody trailing edge (ATE). For the jet-on set of images, the exhaust flow out to the exhaust plume is represented as the dark area of the image. A vortex at all four corners is evident. Expansion of the exhaust plume out onto the inboard section of the horizontal tail appears to start at station number 4. The curved nature of the external plume shock and the inlet fairing shock (the two white shapes below the dark zone) also illustrates the spanwise nature of this aftbody flowfield. The effects of angle-of-attack, AOA, on the exhaust flowfield structure in the spanwise direction are shown by the set of rear-view vapor screen images presented in Fig. 24. The exhaust plume is notably compressed, with more of an

inverted mushroom shape at 6 degrees AOA compared to 0 degrees AOA.

The effect of the exhaust gas γ on the aftbody force and moment data for Model 5B at Mach 10 is presented in Fig. 25a-c through a comparison of results from air versus the CF_4/Ar mixture. Notable differences were apparent, with the differences increasing with increasing SNPR. For an actual scramjet the exhaust γ will be mostly a function of the fuel used and the exhaust temperature at the cowl trailing edge, also referred to as station 4. The effect of M_4 on the aftbody pressure distribution of Model 5B at Mach 10 is shown in Fig. 26. The three different M_4 conditions were achieved through the use of three separate Model 5B internal nozzles, each geometrically designed for a specific M_4. The effect is most pronounced for the M_4 = 2.3 condition. This figure illustrates an example of how the propulsion flowpath internal nozzle design can affect the performance of the aftbody portion of the vehicle airframe. An example of the jet-effect on the effectiveness of the horizontal tails for Model 5B at Mach 6 is presented in Fig. 27. The positive 10 degree horizontal tail deflection is roughly 30 percent more effective at the SNPR = 40 condition than at the jet-off condition. This is a result of the aft portion of the horizontal tail being rotated farther down (for positive deflections) into the exhaust flowfield, which generates higher pressurization/loads on this surface with increasing SNPR. An example of the jet-effect on the external cowl pressure distribution for Model 5B at Mach 3.4 is provided in Fig. 28. For all tested SNPR conditions the exhaust jet is underexpanded (SNPR > 1) generating a plume that expands downward into the external cowl flow and an external plume shock, as shown back in Fig. 22. The strength of this external plume shock is sufficient to separate the external cowl flow within one inch of the CTE, for all SNPR conditions tested. The magnitude of the pressure rise within this separated flow zone increases with increasing exhaust jet SNPR, as expected.

For all supersonic and hypersonic test conditions, Model 5B was tested at SNPR conditions greater than one, yielding an underexpanded exhaust flow at the CTE. These test conditions were derived from bracketing a predicted nominal target operating condition for the NASP vehicle in supersonic and hypersonic flight. For transonic testing of Model 5B a set of nominal target operating conditions was derived from a potential X-43B concept vehicle. There has been an effort within NASA's X-43B project (Ref. 1) to better understand the transonic jet effects on hypersonic airbreathing configurations. Part of this effort involved acquiring powered simulation data on Model 5B at transonic flight conditions. This led to a set of SNPR values all less than one, yielding overexpanded exhaust flow at the CTE. Essentially, this overexpanded exhaust flow at the CTE is a result of operating an internal nozzle, designed for hypersonic flight, at transonic flight conditions. This overexpanded exhaust jet led to some very different exhaust flowfield structure and aftbody pressure distributions than those obtained at Mach 3.4, 6, and 10 for Model 5B.

A photograph of Model 5B installed in the Langley 16-Foot Transonic Tunnel is shown in Fig. 29. Fig. 30a shows a profile view schematic of the overexpanded exhaust flowfield structure at transonic test conditions. The overexpanded flow at the CTE resulted in a plume formation that turned upward towards the external nozzle surface. This upward-turning exhaust plume generated an internal plume shock at the CTE, that impinged on the aftbody surface, and then created a reflected shock off the aftbody. This aftbody reflected shock then intersected the exhaust plume creating a lambda shock formation with a reflected plume shock that subsequently impinged farther down on the aftbody. In the planform view of the aftbody, shown in Fig. 30b, the spanwise nature of this flowfield structure is illustrated. The external nozzle surface experiences a region of continued nozzle expansion of the exhaust flow, followed by a region of pressure rise due to internal plume shock impingement, which is then followed by a region of prominent pressure rise due to the impingement of the reflected plume shock onto the aftbody. An example external nozzle pressure distribution for Model 5B at transonic test conditions (Mach = 0.95) is presented in Fig. 31a. This plot shows four streamwise rows of pressure data from the centerline out to the outboard edge of the external nozzle. This data clearly indicates the region of continued nozzle expansion followed by an initial pressure rise (due to the internal plume shock) and then a secondary, more prominent pressure rise (due to the reflected plume shock). This data also reveals that the initiation of these two regions of pressure rise are a function of spanwise location. The three-dimensional nature of the external nozzle surface pressure distribution is quite evident in Fig. 31b, a contour plot created from all of the pressure data from the aftbody of Model 5B for this same test point. In this contour plot, the spanwise pressure variation starts, as expected, at the trailing edge of the nozzle sidewall and then propagates inboard. This is due to the higher pressure external flow turning inward into the lower pressure exhaust jet. A profile-view shadowgraph showing the aftbody exhaust flowfield structure for this transonic test point is presented in Fig. 31c.

For this Model 5B transonic test, powered exhaust simulation data was acquired over a Mach number range from 0.7 to 1.2 for a range of SNPR conditions and AOA values around the predicted nominal flight conditions. Centerline external nozzle pressure distributions from just the flight condition test points are presented in Fig. 32a. The location of the X-43B aftbody trailing edge, based upon cowl exit height scaling of X-43B to Model 5B scale, is indicated in this figure. This data reveals a major PAI concern for transonic flight of this X-43B concept. The pressure distribution varies considerably for the X-43B portion of the external nozzle from Mach 0.7 to Mach 1.2. At Mach 0.7 the external nozzle pressure data indicates the presence of both the internal plume shock and the reflected plume shock for the X-43B aftbody. At Mach 1.2 the external nozzle pressure data indicates only the existence of the exhaust flow nozzle expansion up to the location of the X-43B aftbody trailing edge. The pressure data for the entire X-43B aftbody portion of Model 5B was integrated to yield the X-43B aftbody normal force, axial force, and pitch moment. These results are presented in Fig. 32b. They indicate a wide range of loads for the external nozzle surface of X-43B from Mach 0.7 to Mach 1.2, as expected from the data shown in Fig. 32a. In particular, the large variation of pitch moment over this transonic speed regime indicates this X-43B configuration would require significant transonic trim capability. This is a concern from the standpoint of the size requirements for the horizontal tails and/or body flaps to achieve this trim capability, and from the standpoint of the large trim drag penalty that will have to be incurred as a result of these control surface deflections.

FULL-LENGTH/WIDTH PROPULSION FLOWPATH TESTS

Technique Description

Full-length/width propulsion flowpath test models can be used to investigate the entire spectrum of PAI issues related to hypersonic airbreathing vehicles. Since these test models are complete tip-to-tail models of the flight vehicle propulsion flowpath and airframe lower surface, no simulation techniques are required, as with the other three previously discussed PAI test techniques. This kind of test model can address all of the PAI issues addressed by the other three PAI test techniques, as well as some additional PAI issues. These additional issues include examination of the three-dimensional, full-length forebody effects on the inlet operability and performance, full-width inlet cowl flap "delta" loads (closed-to-open), and multi-module engine effects. Due to the cost of these test models, the testing costs for the large-scale facilities in which they are tested, and the lower test productivity of such large-scale facilities, only PAI issues that cannot be adequately addressed by one of the other three PAI test techniques are addressed with the full-length/width propulsion test models.

A photograph of a Hyper-X full-length/width propulsion flowpath test model, known as the Hyper-X Flight Engine with Vehicle Flowpath Simulator (HXFE/VFS) is shown, mounted inverted on its pedestal, during a test at Mach 7, in Fig. 33a.[13] The HXFE/VFS, a full-scale model of the Hyper-X flight vehicle, was tested in the Langley 8-Foot High Temperature Tunnel (8-Ft. HTT) at Mach 7 flight conditions to address PAI issues as well as to verify predicted propulsion performance and to verify the functionality of several propulsion subsystems prior to flight demonstration. A three-view schematic of the HXFE/VFS is provided in Fig. 33b. This model was used to verify the computational prediction for closed-to-open cowl flap increments, to verify the magnitude of the exhaust jet effect on the aftbody, and to determine the spanwise extent of the exhaust jet expansion onto the aftbody and control surfaces.

Fig. 34a shows a three-dimensional schematic of another full-length/width propulsion flowpath test model know as the Multi-module Flowpath Propulsion Demonstrator (MFPD). The MFPD is a 2/3 scale, tip-to-tail, propulsion flowpath model of the X-43C. This test model, slated for testing in the 8-Ft. HTT, is currently in the design and fabrication stage. The primary test objectives for the MFPD are the assessment of the inlet operability and performance with a full three-dimensional forebody, the module-to-module interactions with the three module engine design of the X-43C, and the exhaust jet-effect on the external nozzle and horizontal tails of the vehicle aftbody. Fig. 34b shows a close-up view of the MFPD three-module inlet, with the cowl flap for the center module in the full-open position and the cowl flaps for the outboard modules in the full-closed position. With independent cowl flap control, the MFPD will be used to investigate single module unstart, flameout, and relight dynamics for both the center and outboard engine modules. Fig. 35a and Fig. 35b show the MFPD inverted, mounted atop its pedestal, which sits on an AOA system in the 8-Ft. HTT. The AOA system will enable a real-time variation of the MFPD AOA from 0 to 8 degrees. This real-time variation of AOA for the MFPD translates to a real-time variation of inlet conditions (M_{CLE}, mass capture, etc.) for the MFPD, providing an opportunity to challenge the propulsion

control system to maintain proper fuel flow rates to avoid both unstart and flameout conditions.

Illustration of PAI Effects

While again, internal propulsion flowpath data cannot be presented in this paper due to its classification, a sample of some unclassified PAI data from the HXFE/VFS test model is presented. Fig. 36 presents a comparison of the longitudinal force and moment coefficients (with no horizontal tail deflections) for the cowl-closed, cowl-open unfueled, and cowl-open fueled conditions. The database estimates, shown by the solid symbols, were developed by applying the computed cowl-opening and power-on increments to the experimentally derived aerodynamic database for the cowl-closed configuration. The increments between the three sets of curves in each coefficient plot represent the differences in the force and moment values between the unfueled and fueled cowl-open conditions. The force and moment increments acquired from the 8-Ft. HTT test data are applied to the same cowl-closed aerodynamic wind-tunnel data to create the HXFE/VFS data and are shown by the open symbols. In general, there was very good agreement between the estimated and measured increments. These results were significant because they built confidence in the Hyper-X preflight database methodology, as well as demonstrated there was a significant effect of forebody/inlet and aftbody pressurization that affected the propulsion flowpath forces and moments, and thus the requirements for trimming the vehicle.

Fig. 37 shows the lateral extent of the plume expansion on the HXFE/VFS aftbody, evident from the deposition of silicon dioxide (SiO_2, a white particulate and byproduct of the reaction of the silane/hydrogen ignition combustion process). The plume is seen to extend laterally outward beyond the cusp line that defines the aftbody nozzle surface. Vortical flow exists with a separation/reattachment region shown, as evidenced by the lack of SiO_2 just outside, and nearly parallel to, the cusp lines.

Fig. 38a and Fig. 38b illustrate the effect of opening the cowl flap and fueling the engine, respectively, on the aftbody pressure distribution. These results are presented in pressure-difference contour plots (in coefficient form) for the aftbody. Pressure-difference refers to the difference between cowl-open and cowl closed for Fig. 38a, and to the difference between fuel-on and fuel-off for Fig. 38b. These results indicate the magnitude of the aftbody contribution to the cowl-opening and fueling increments in Fig. 36.

SUMMARY

The scope and significance of PAI for hypersonic airbreathing vehicles has been presented through a discussion of the PAI test techniques utilized at NASA Langley Research Center to acquire an understanding of this discipline. An examination of each of the four primary types of PAI model tests utilized at NASA Langley for hypersonic airbreathing vehicles was presented. The four types of PAI test models examined were the forebody/inlet test model, the partial-width/truncated propulsion flowpath test model, the powered exhaust simulation test model, and the full-length/width propulsion flowpath test model. The test technique for each of these four types of PAI test models was described and the relevant PAI issues addressed by each test technique were illustrated through the presentation of recent PAI test data.

The forebody/inlet test model was used for the examination of the forebody-processed flow effect on inlet performance. Specific PAI issues addressed by this technique were forebody boundary layer, inlet mass capture, unstart loads, and inlet operability limits. The partial-width/truncated propulsion flowpath test model was used for the examination of the forebody-processed flow effect on the entire internal propulsion flowpath. In addition to the PAI issues addressed by the forebody/inlet test model, this test model could also address the issues of isolator interaction and propulsion system control. The powered exhaust simulation test model was used for the examination of the engine exhaust jet interaction with the external nozzle and control surfaces of the vehicle aftbody. Some specific PAI issues addressed by this test model were vehicle stability and control for powered flight, powered trim drag penalties, and exhaust jet conditions at the internal nozzle exit. Lastly, the full-length/width propulsion flowpath test model was used for examination of the entire spectrum of PAI issues related to hypersonic airbreathing vehicles, although test costs with this technique are a limiting factor. Some PAI issues that can only be addressed by this test model are full-length, three-dimensional forebody effects, full-width cowl flap loads, and multi-module engine effects.

REFERENCES

1. Covault, C., "Hypersonics Strategy Sets Stage for 'Next Great Step'", *Aviation Week & Space Technology*, March 26, 2001, pp 28-29.

2. Andrews, Earl H., and Mackley, Ernest A., NASA's Hypersonic Research Engine Project – A Review. NASA TM 107759, October 1994.

3. Rock, K. E., Voland, R. T., Rogers, R.C., and Huebner, L. D., "NASA's Hyper-X Scramjet Engine Ground Test Program", International Symposium on Air Breathing Engines, ISABE Rept. 99-7214, September 1999.

4. Morring, F. Jr., "NASA Drawing New Launch Road Map", *Aviation Week & Space Technology*, January 27, 2003, pp 60-61.

5. Smart, M. K., "Experimental Testing of a Hypersonic Inlet with Rectangular-to-Elliptical Shape Transition", *Journal of Propulsion and Power*, Vol. 17, No. 2, pp 276-283, 2001.

6. Rausch, V. L., McClinton, C. R., and Sitz, J. R., "The Hyper-X Program Overview", International Symposium on Air Breathing Engines, ISABE Rept. 97-7024, Sept. 1997.

7. Guy, R. W., Rogers, R. C., Puster, R. L., Rock, K. E., and Diskin, G. S., "The NASA Langley Scramjet Test Complex", AIAA Paper 96-3243, July 1996.

8. Hodge, J. S., and Harvin, S. F., "Test Capabilities and Recent Experiences in the NASA Langley 8-Foot High Temperature Tunnel", AIAA Paper 2000-2646, June 2000.

9. Wilhite, A. W., Powell, R. W., Scotti, S. J., McClinton, C. R., Pinckney, S. Z., Cruz, C. I., Jackson, L. R., Hunt, J.L., Cerro, J. A., and Moses, P. L., "Concepts Leading to the National Aero-Space Plane Program", AIAA Paper 90-0294, January 1990.

10. Capone, F. J., Bangert, L. S., Asbury, S. C., Mills, T. L., and Bare, E. A., The NASA Langley 16-Foot Transonic Tunnel. NASA TP 3521, Sept 1995.

11. Jackson, C. M. Jr., Corlett, W. A., and Monta, W. J., Description and Calibration of the Langley Unitary Plan Wind Tunnel. NASA TP 1905, 1981.

12. Miller, C. G., "Langley Hypersonic Aerodynamic/Aerothermodynamic Testing Capabilities – Present and Future", AIAA Paper 90-1376, June 1990.

13. Huebner, L. D., Rock, K. E., Ruf, E. G., Witte, D. W., and Andrews, E. H. Jr., "Hyper-X Flight Engine Ground Testing for Flight Risk Reduction", *Journal of Spacecraft and Rockets*, Vol. 38 No. 6 pp 844-852, 2001.

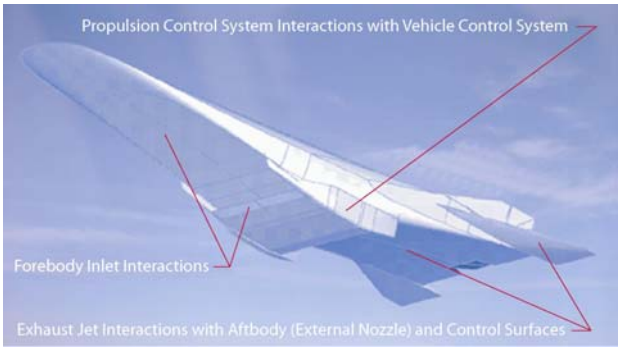

Fig. 1 Primary PAI issues for an airframe-integrated scramjet powered aircraft.

Fig. 2 X-43C forebody/inlet model in LaRC M4BDF.

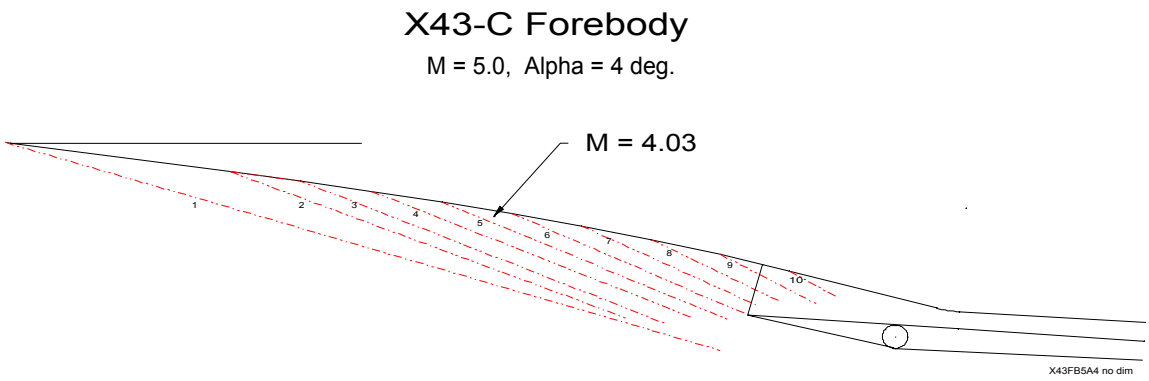

Fig. 3 X-43C forebody shock locations.

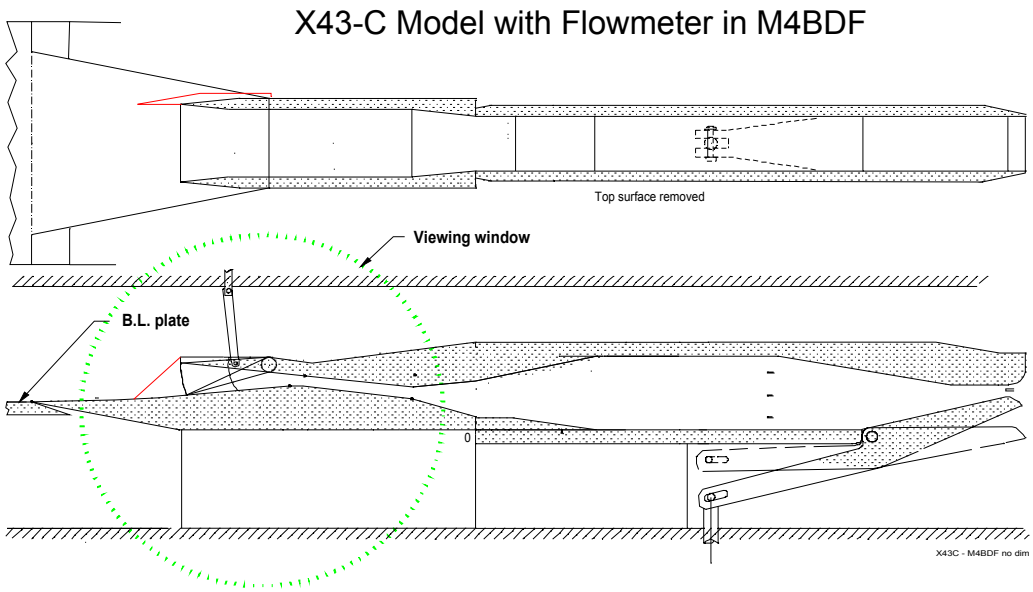

Fig. 4 Profile and planform schematics (inverted) for the X-43C forebody/inlet model in the LaRC M4BDF.

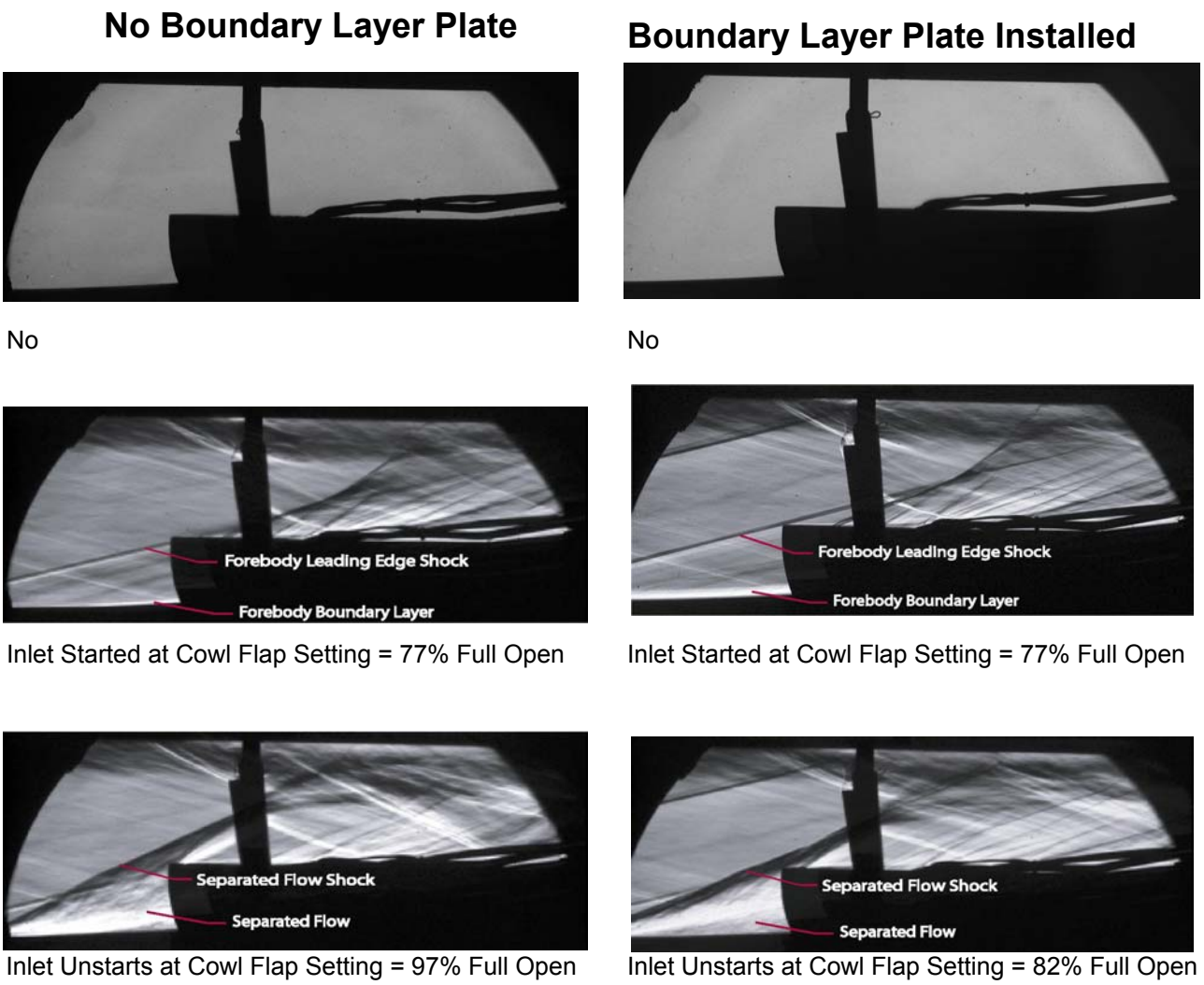

Fig. 5 Schlieren photographs for X-43C forebody/inlet model in LaRC M4BDF with and without a boundary layer plate.

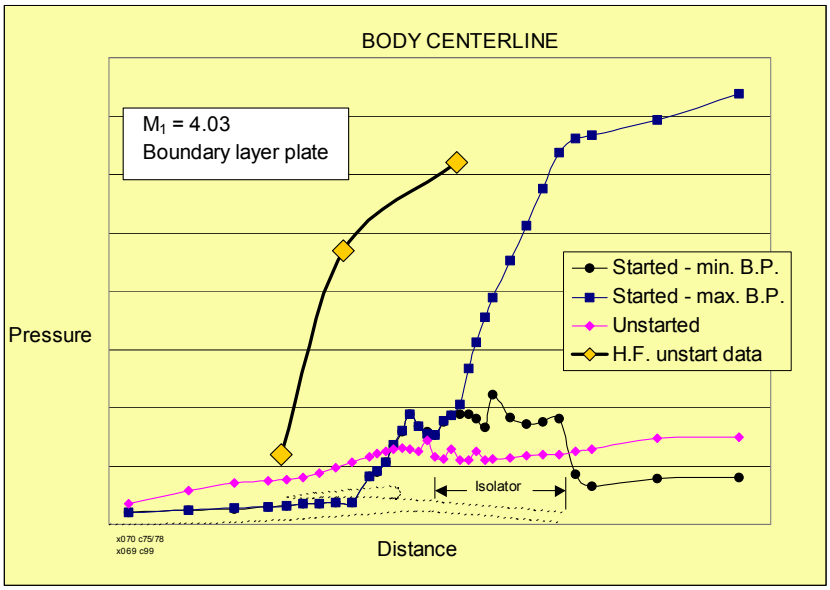

Fig. 6 Static and dynamic pressure data from the X-43C forebody/inlet model for both started and unstarted inlets.

Fig.7 The REST forebody/inlet model.

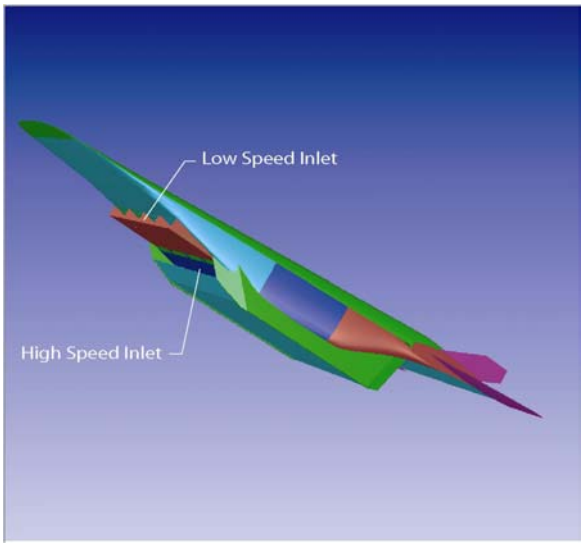

Fig. 8 A TBCC dual flowpath (over/under) concept.

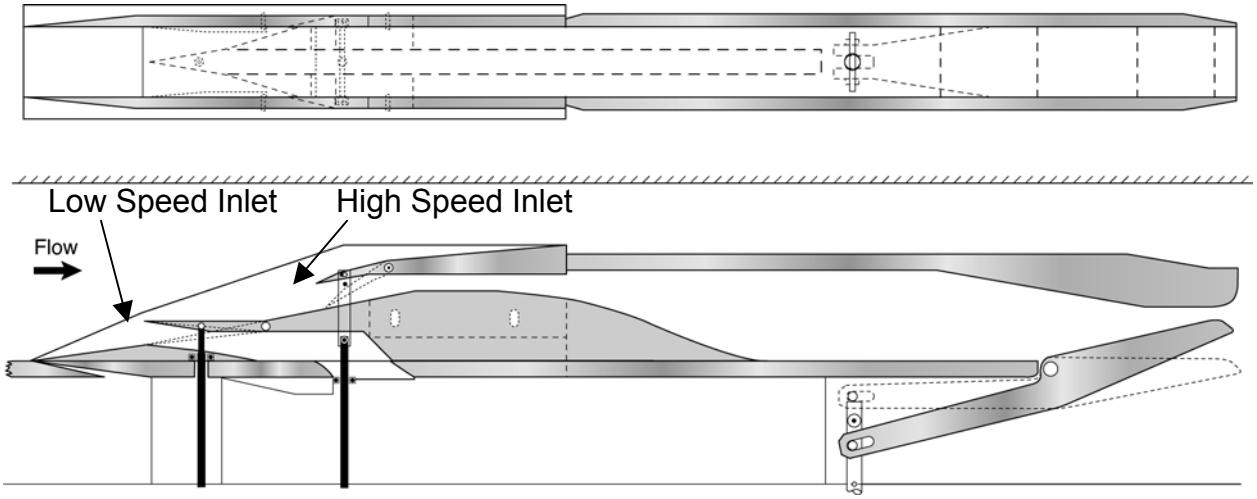

Fig. 9 Planform and profile schematics for the TBCC dual flowpath forebody/inlet model (shown inverted).

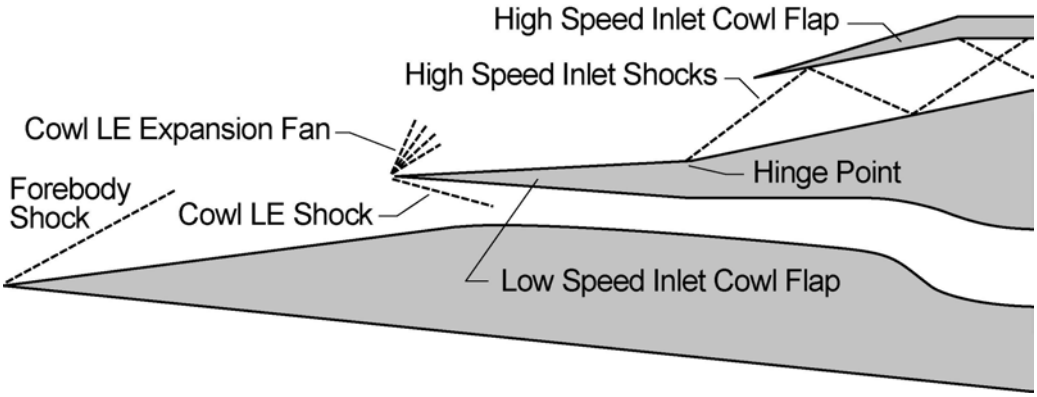

Fig. 10 Shock diagram for the TBCC over/under inlet configuration (shown inverted).

Fig. 11 Hyper-X DFX model in the LaRC AHSTF.

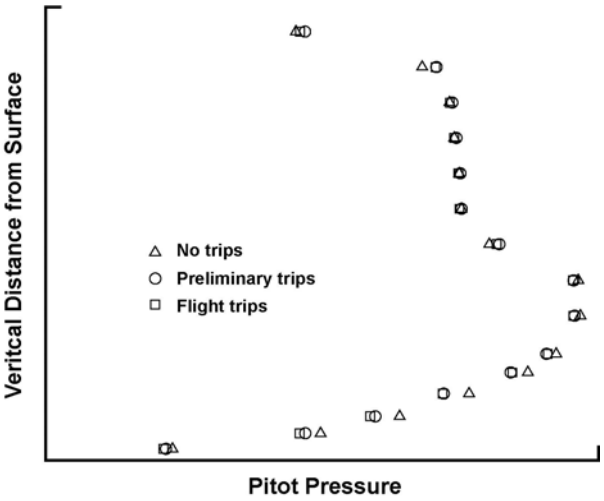

Fig. 14 Effect of boundary layer trips on pitot pressure measurements.

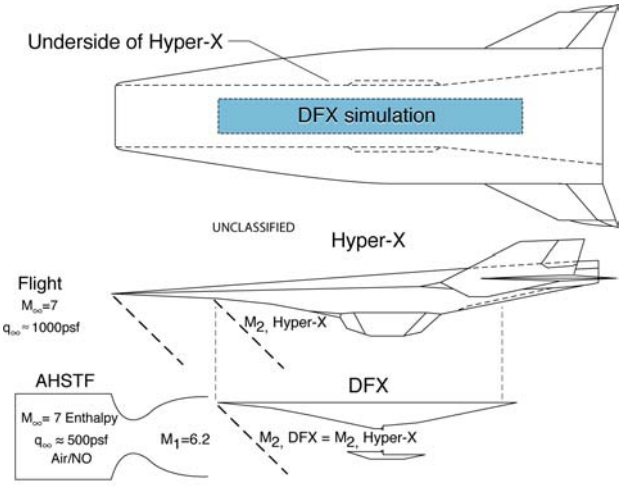

Fig. 12 Comparison of DFX simulation to flight.

Fig. 15 HXEM without forebody boundary layer diversion.

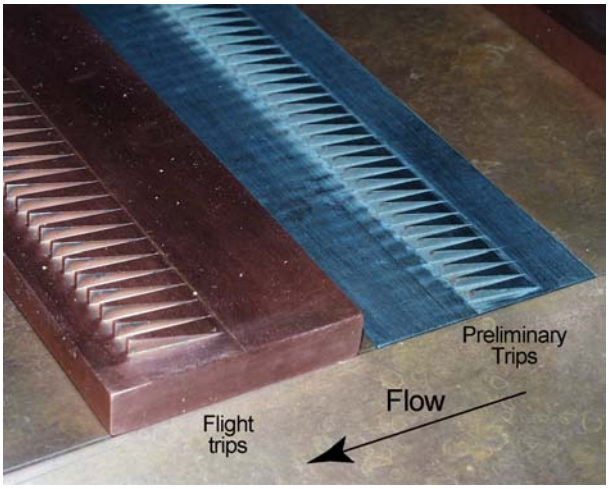

Fig. 13 Comparison of forebody boundary layer trips.

Fig 16 HXEM with forebody boundary layer diversion.

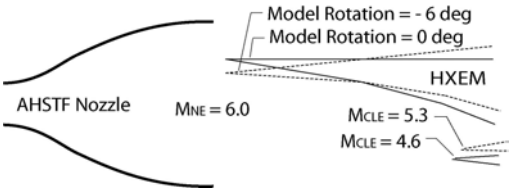

Fig. 17 Range of M_{CLE} tested for the HXEM.

Fig. 18 HXEM with forebody flow survey rakes.

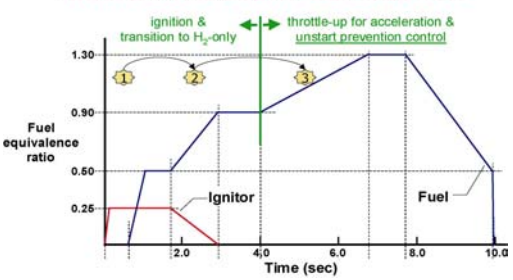

Fig. 19 Hyper-X fuel and ignitor sequence.

Fig. 20 NASP Model 5B, a powered exhaust simulation model.

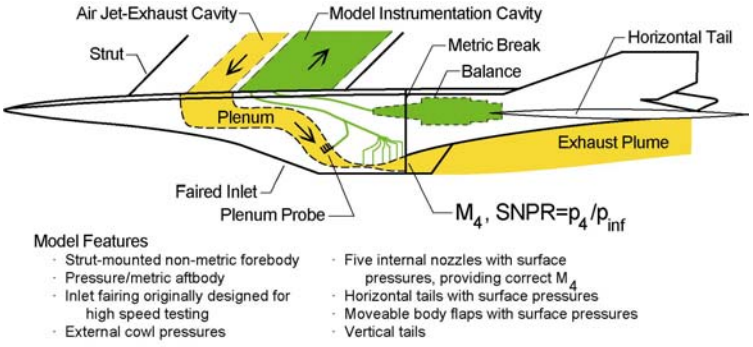

Fig. 21 Profile schematic of Model 5B internal features.

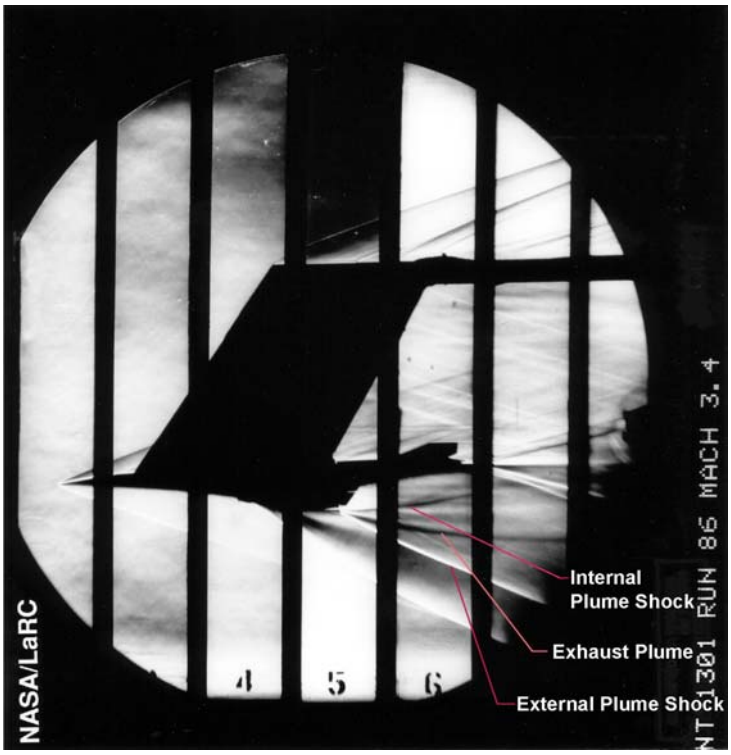

Fig. 22 Schlieren photograph of Model 5B at Mach 3.4.

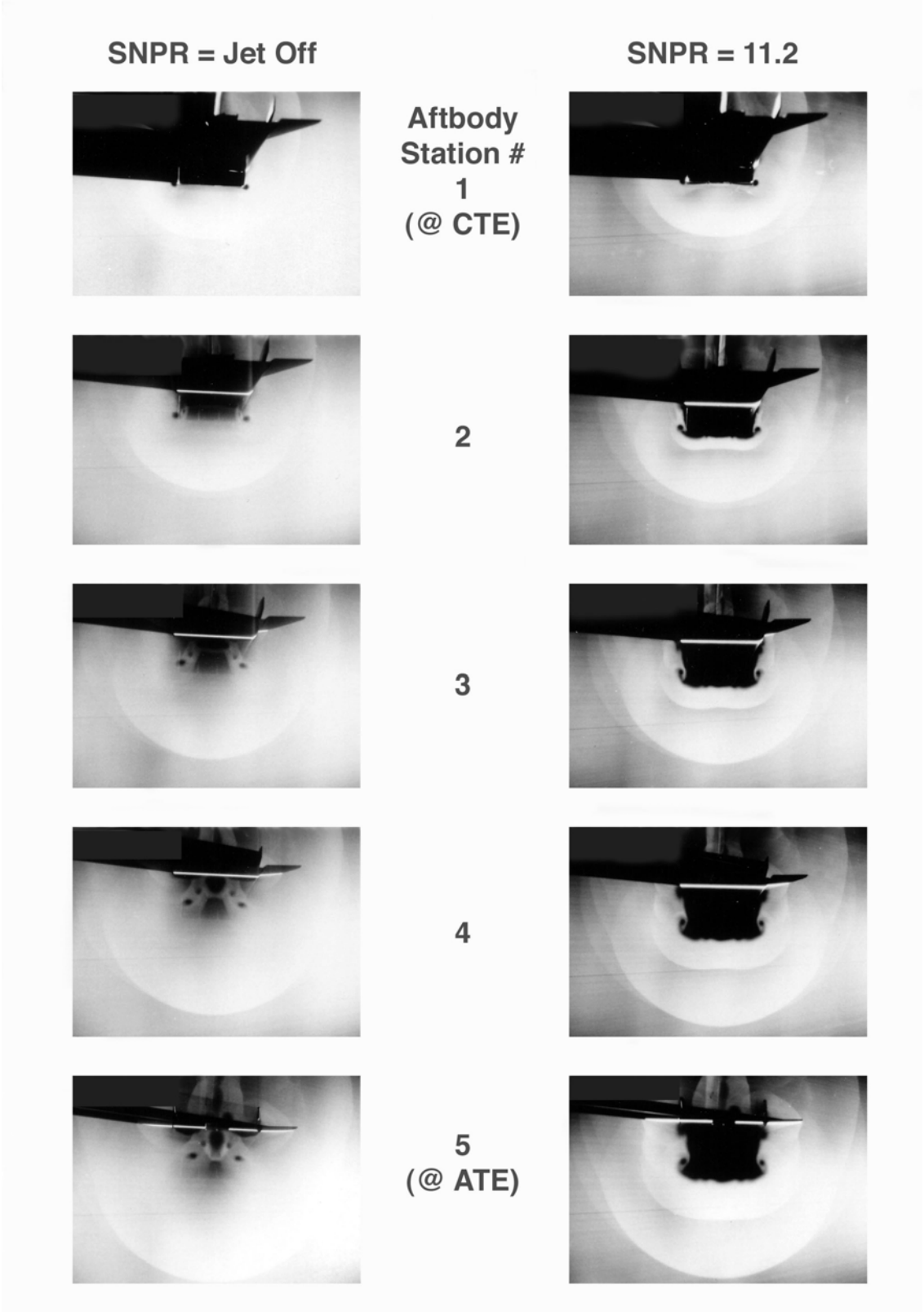

Fig. 23 Rear-view vapor screen images of Model 5B at Mach 3.4 comparing jet-on to jet-off effects (all other conditions constant).

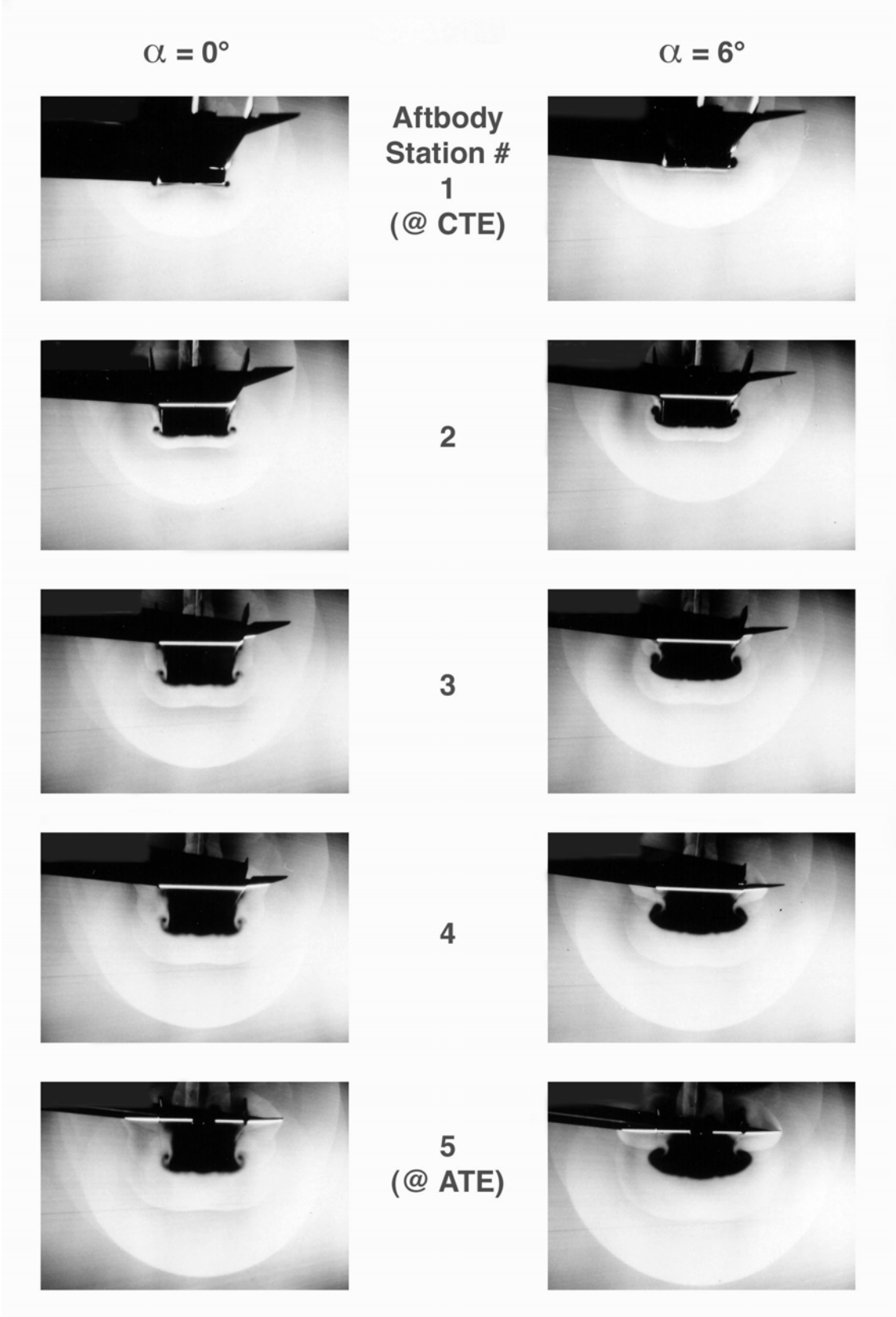

Fig. 24 Rear-view vapor screen images of Model 5B at Mach 3.4 illustrating angle-of-attack effects (all other conditions constant).

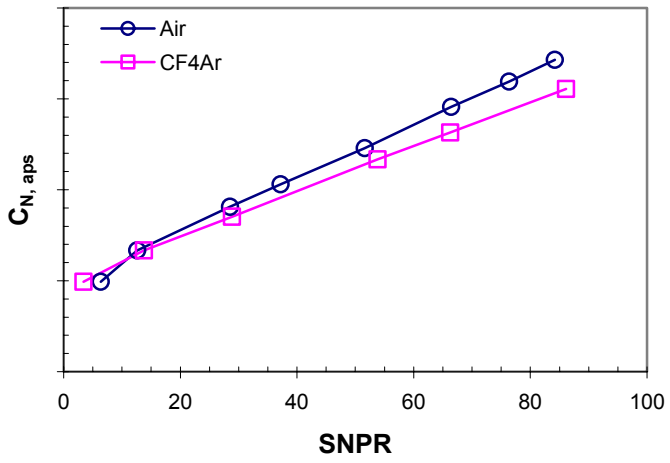

Fig.25a Exhaust gas γ effect on normal force coefficient for Model 5B at Mach 10.

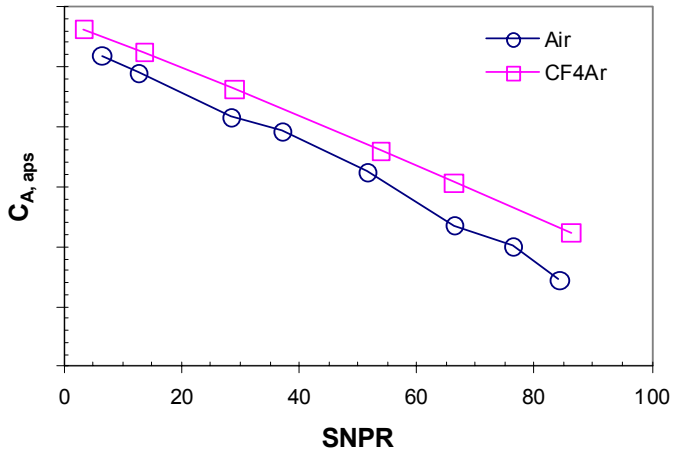

Fig. 25b Exhaust gas γ effect on axial force coefficient for Model 5B at Mach 10.

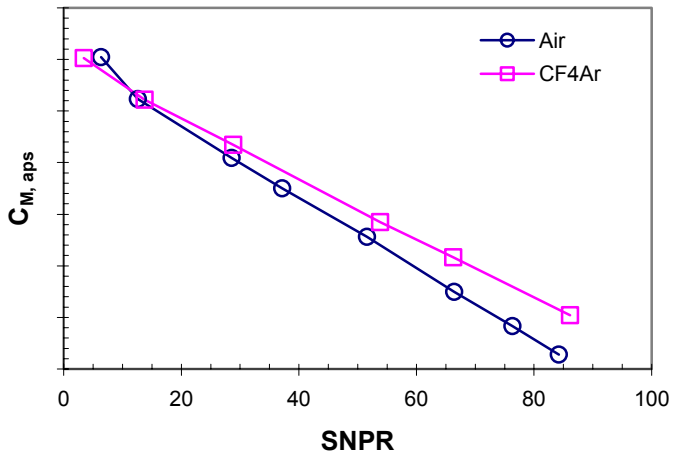

Fig. 25c Exhaust gas γ effect on pitch moment coefficient for Model 5B at Mach 10.

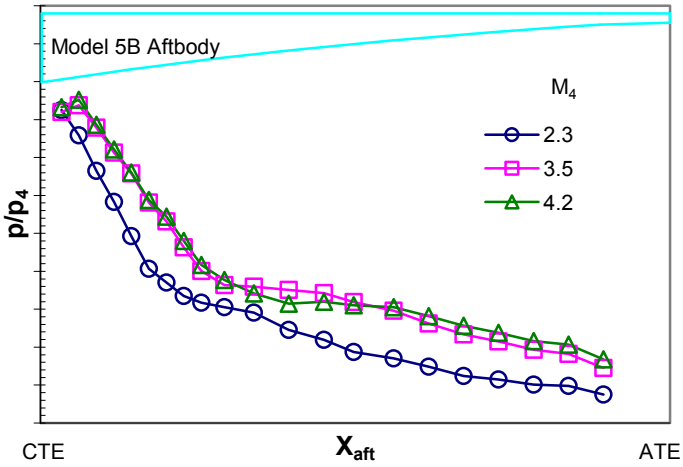

Fig. 26 Effect of CTE Mach number on aftbody pressure distribution for Model 5B at Mach 10.

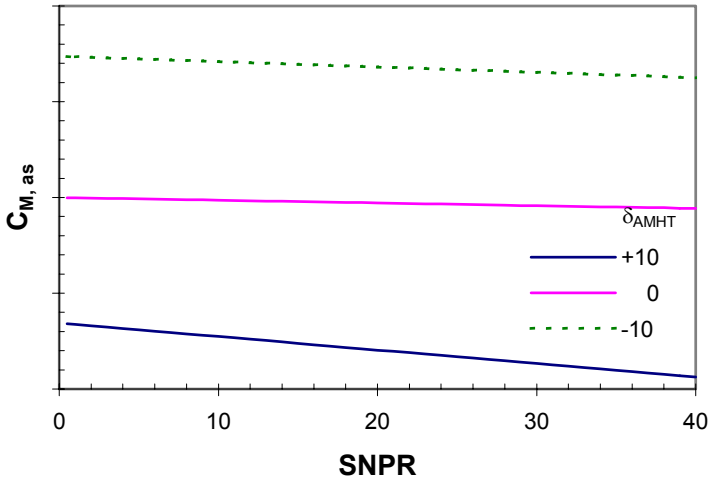

Fig. 27 Jet-effect on the horizontal tail control effectiveness for Model 5B at Mach 6.

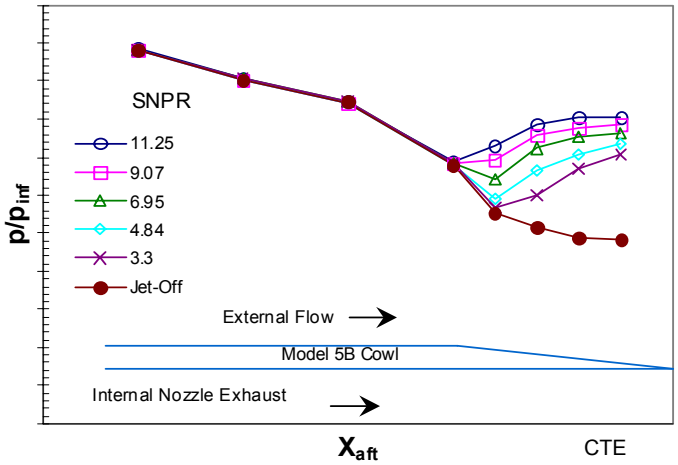

Fig. 28 Jet-effect on the external cowl surface pressure distribution for Model 5B at Mach 3.4.

Fig. 29 Model 5B in Langley 16-Ft Transonic Tunnel.

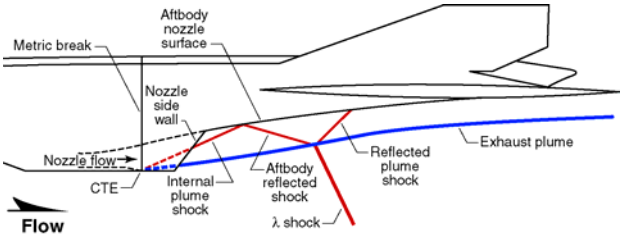

Fig. 30a Profile view schematic of overexpanded exhaust flowfield structures at transonic test conditions.

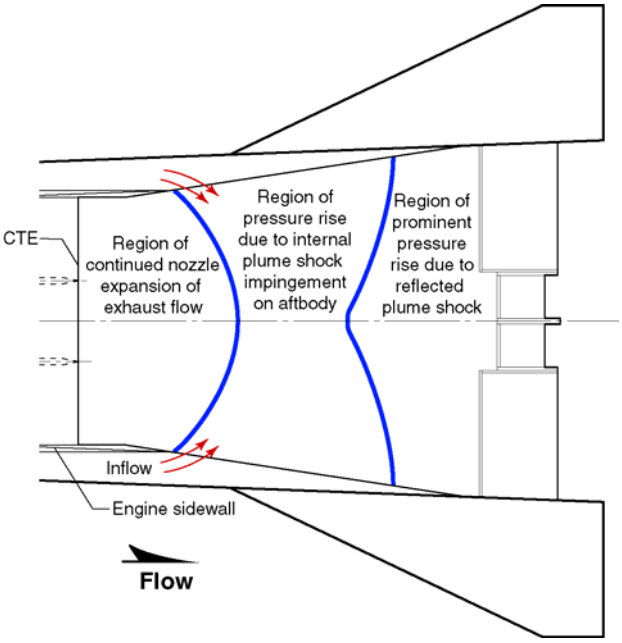

Fig. 30b Planform view schematic of overexpanded exhaust flowfield structures at transonic test conditions.

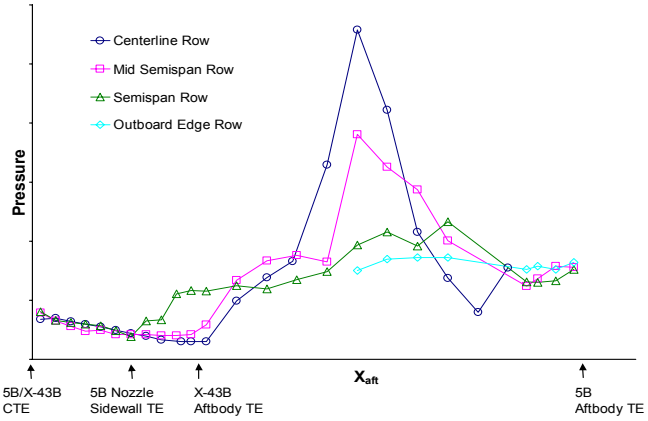

Fig. 31a External nozzle pressure distribution for Model 5B at Mach 0.95.

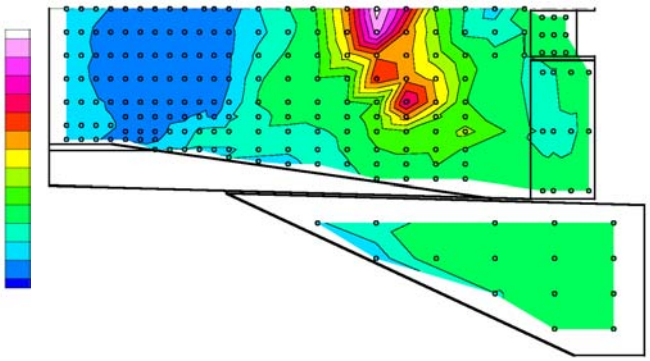

Fig. 31b Aftbody pressure contour plot for Model 5B at Mach 0.95.

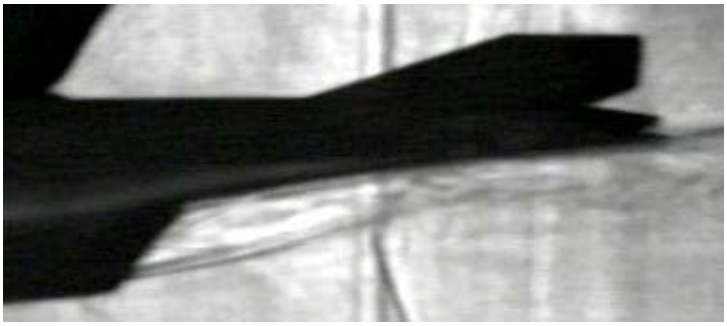

Fig. 31c Profile-view shadowgraph of Model 5B aftbody and exhaust flowfield at Mach 0.95

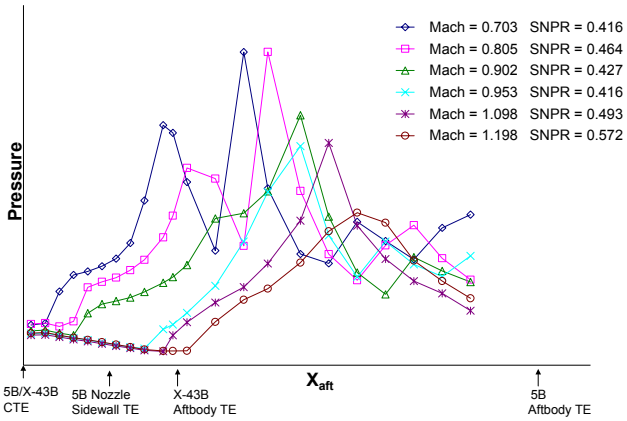

Fig. 32a Model 5B centerline external nozzle pressure distributions for X-43B transonic flight test conditions.

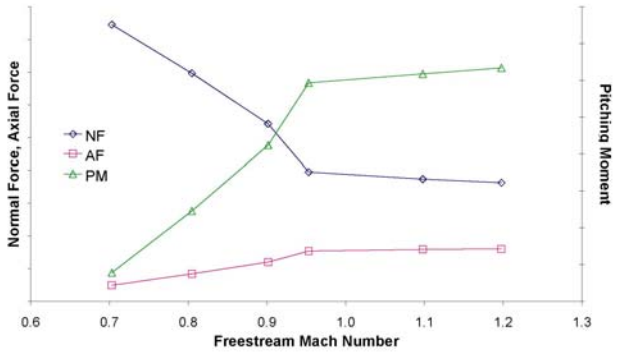

Fig. 32b Pressure-integrated external nozzle force and moment results for the X-43B portion of the Model 5B aftbody at transonic flight test conditions.

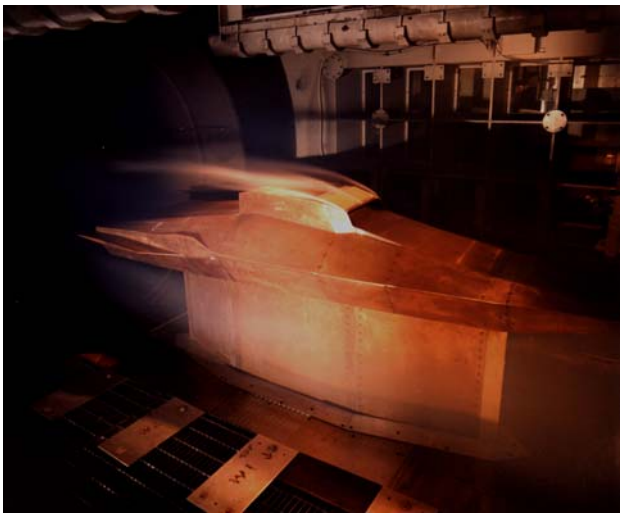

Fig. 33a HXFE/VFS in the 8-Ft. HTT at Mach 7.

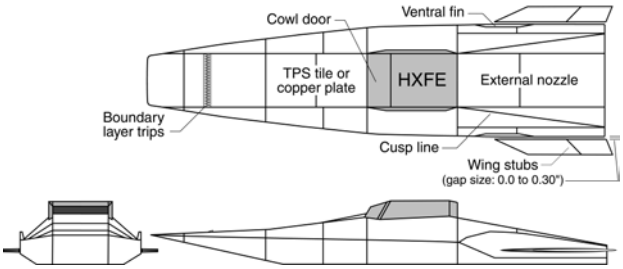

Fig. 33b Three-view schematic of HXFE/VFS.

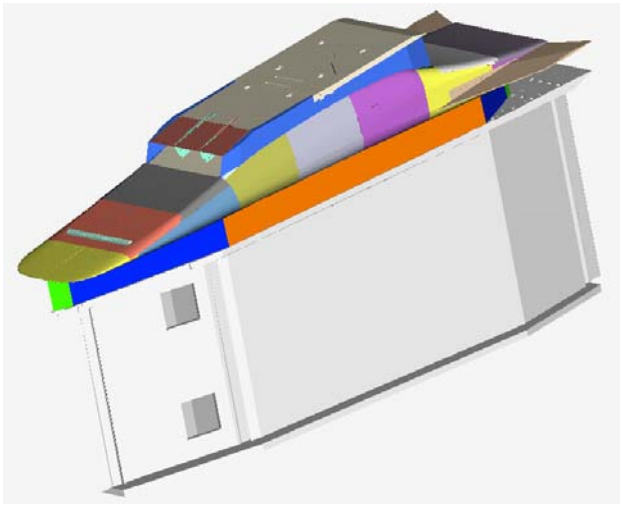

Fig. 34a Three-dimensional schematic of MFPD.

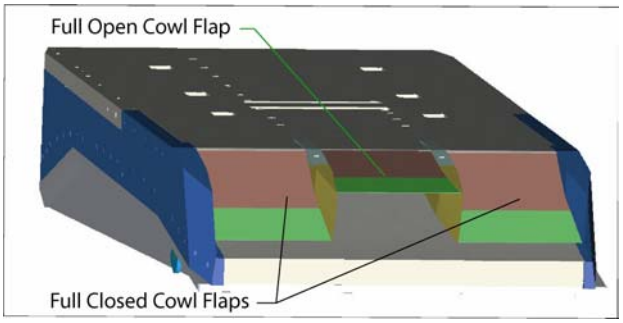

Fig. 34b MFPD three-module engine.

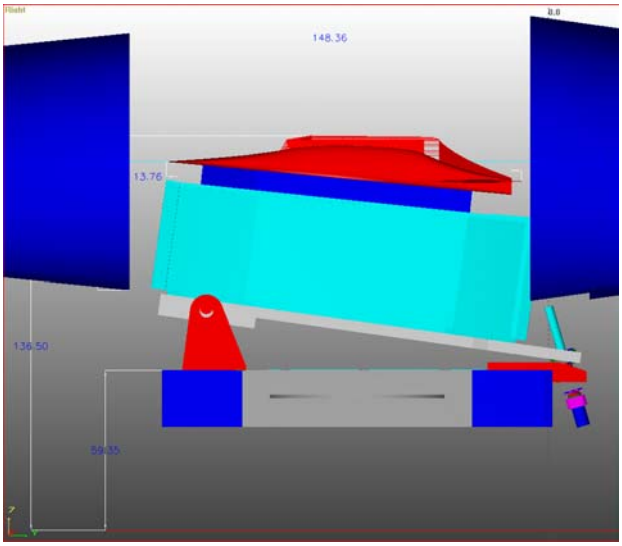

Fig. 35a MFPD at AOA = 0 degrees.

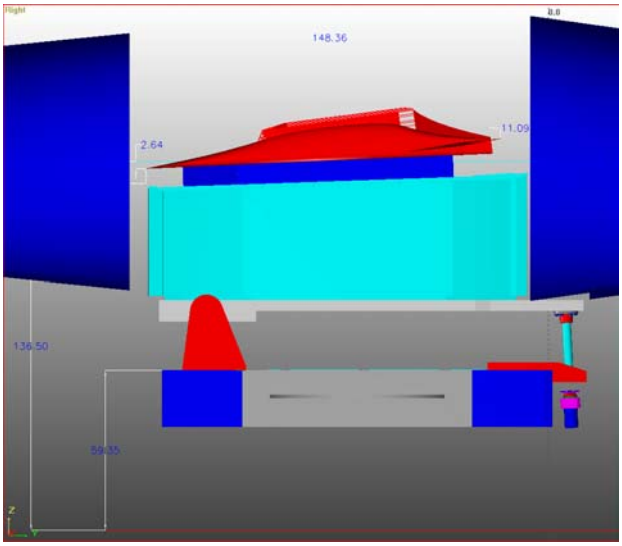

Fig. 35b MFPD at AOA = +8 degrees.

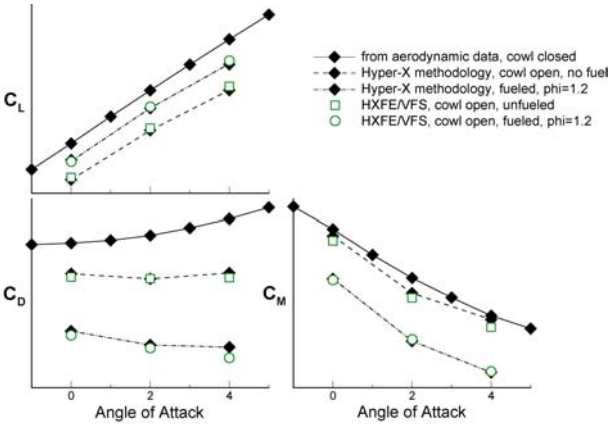

Fig. 36 Cowl-opening and fueling effect on Hyper-X.

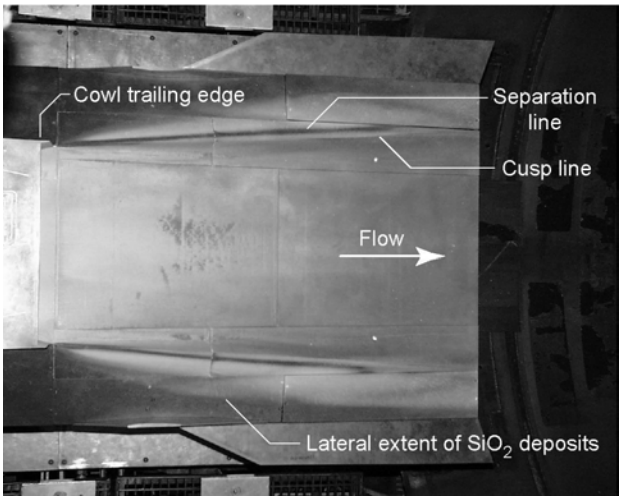

Fig. 37 SiO_2 deposits on HXFE/VFS aftbody following a fueled run.

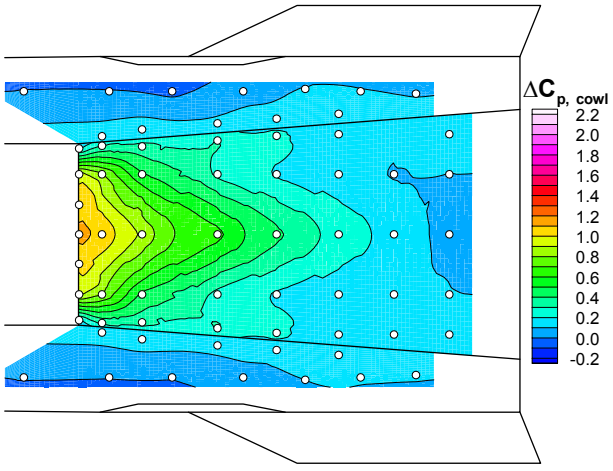

Fig. 38a HXFE/VFS aftbody pressure change due to cowl-opening.

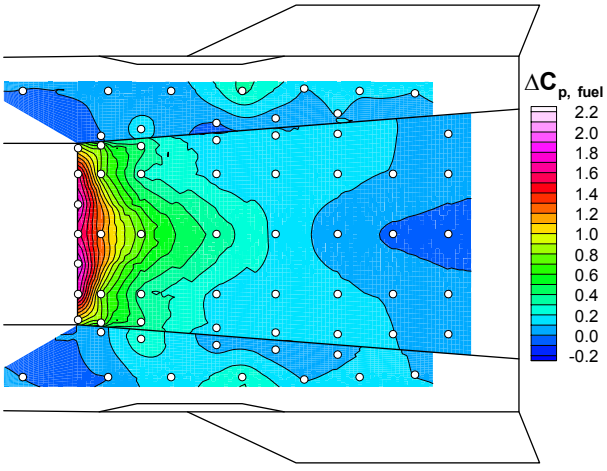

Fig. 38b HXFE/VFS aftbody pressure change due to fueling.